J. Fluid Mech. (1989), *vol.* 206, *pp.* 105–129
Printed in Great Britain

The viscous flow on surfaces with longitudinal ribs

By D. W. BECHERT AND M. BARTENWERFER
DLR, Abteilung Turbulenzforschung, Müller-Breslau-Straße 8, 1000 Berlin-West 12, West Germany

(Received 29 June 1988 and in revised form 13 January 1989)

The viscous sublayer of a turbulent boundary layer on a surface with fine longitudinal ribs (riblets) is investigated theoretically. The mean flow constituent of this viscous flow is considered. Using conformal mapping, the velocity distributions on various surface configurations are calculated. The geometries that were investigated include sawtooth profiles with triangular and trapezoidal grooves as well as profiles with thin blade-shaped ribs, ribs with rounded edges and ribs having sharp ridges and U-shaped grooves. (This latter riblet configuration is also found on the tiny scales of fast sharks.) Our calculations enable us to determine the location of the origin of the velocity profile that lies somewhat below the tips of the ridges. The distance between this origin and the tip of the ridge we call 'protrusion height'. The upper limit for the protrusion height is found to be 22% of the lateral rib spacing; the coefficient 0.22 being the value of the expression $\pi^{-1} \ln 2$. This limit is valid for two-dimensional riblet geometries. Analogous experiments with an electrolytic tank are carried out as an additional check on the theoretical calculations. This is also an easy way to determine experimentally the location of the origin of the velocity profile for arbitrary new riblet geometries. A possible connection between protrusion height and drag reduction in a turbulent boundary layer flow is discussed. Finally, the present theory also produces an orthogonal grid pattern above riblet surfaces which may be utilized in future numerical calculations of the whole turbulent boundary layer.

1. Introduction

The flow on surfaces with fine longitudinal ribs has become a subject of scientific research because these non-planar surfaces are capable of reducing the shear stress of a turbulent boundary layer to below that of a smooth surface.

Historically, there is no doubt that nature has a clear priority for the development of drag-reducing surfaces. The skin of fast sharks is covered with tiny scales which have little longitudinal ribs on their surface. Shark scales with this structure have been found in fossils more than 100 million years old (Reif 1985). In spite of the fact that the particular shape of shark scales has been known to biologists for more than a century, the first authors to speculate about their fluid dynamical significance were Russian scientists in the late sixties (Burdak 1969; Chernyshov & Zayets 1970). Unfortunately, at that time fluid dynamics was not sufficiently advanced to provide sensible explanations for the particular scale shapes visible under the microscope. In the meantime, however, the body of knowledge on shark scales has been increased considerably (Reif 1982, 1985; Reif & Dinkelacker 1982; Rashi & Musick 1984). In figure 1 the scale pattern of a fast shark can be seen, compared to that of a slow shark in figure 2. The photographs in these figures are taken from the work of Reif (1985) and the drawings are taken from the book on sharks by Steuben & Krefft (1978).

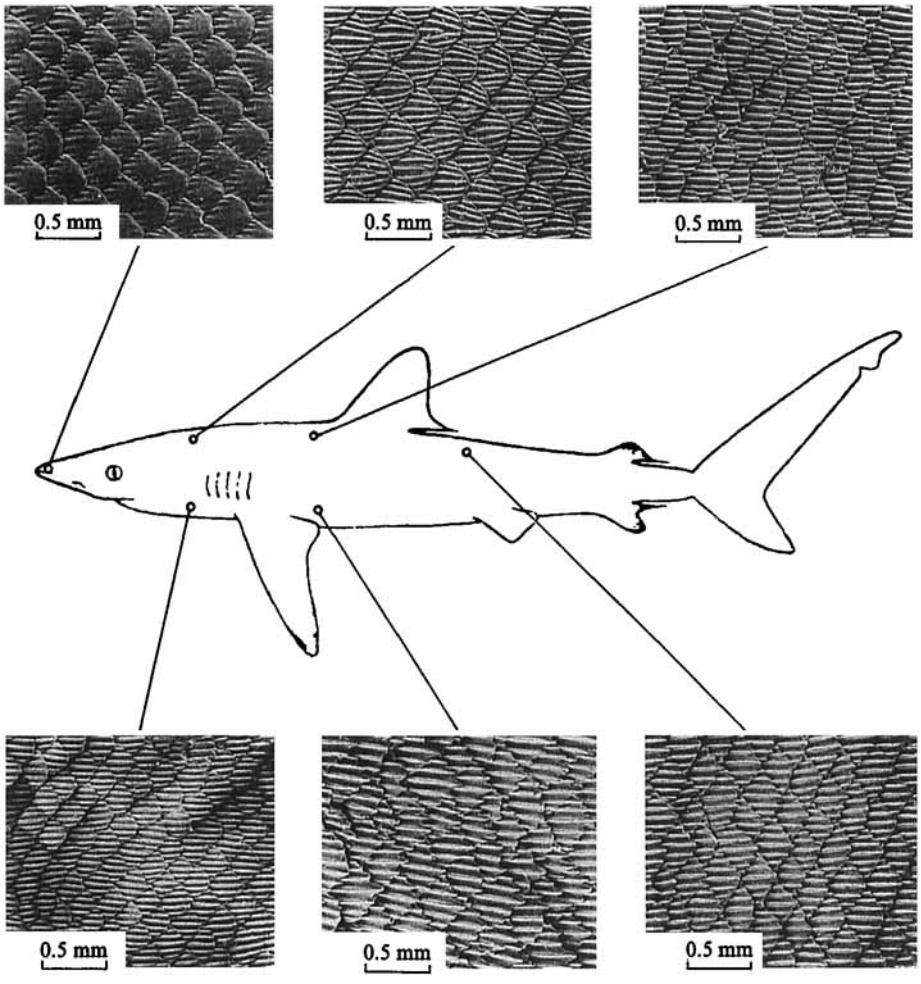

FIGURE 1. Silky shark, *Carcharhinus falciformis*, 2.27 m length.

Until the late seventies, this issue had escaped the scrutiny of the community of fluid dynamicists. This was partly due to the very fine structure of the shark scales which can only be seen using a microscope. Also, it was considered impossible to devise a surface having less friction drag in a turbulent boundary layer than that produced by a smooth surface. Eventually, the situation changed when details of the flow pattern of the viscous sublayer of a turbulent boundary layer became clearer. The first documentation of this particular flow pattern was provided by Hama (see Corrsin 1956, figure 15, p. 394). More detailed investigations were carried out in the sixties by Kline and his coworkers (see e.g. Kline *et al.* 1967), and later by Smith and his coworkers (see e.g. Smith & Metzler 1983). It has been shown by these authors that the viscous sublayer exhibits a streaky structure with local regions of low velocity, extending in the streamwise direction. One hypothesis to explain these 'low-speed streaks' is that they are produced by slowly rotating longitudinal vortices. There is some evidence to support this idea, for example the flow visualization photographs by Cantwell (in Coles 1978, see also Van Dyke 1982, p. 93) and the theoretical investigations by Jang, Benney & Gran (1986). On the other hand, it has been suggested that this streaky structure belongs to a 'hairpin' vortex.

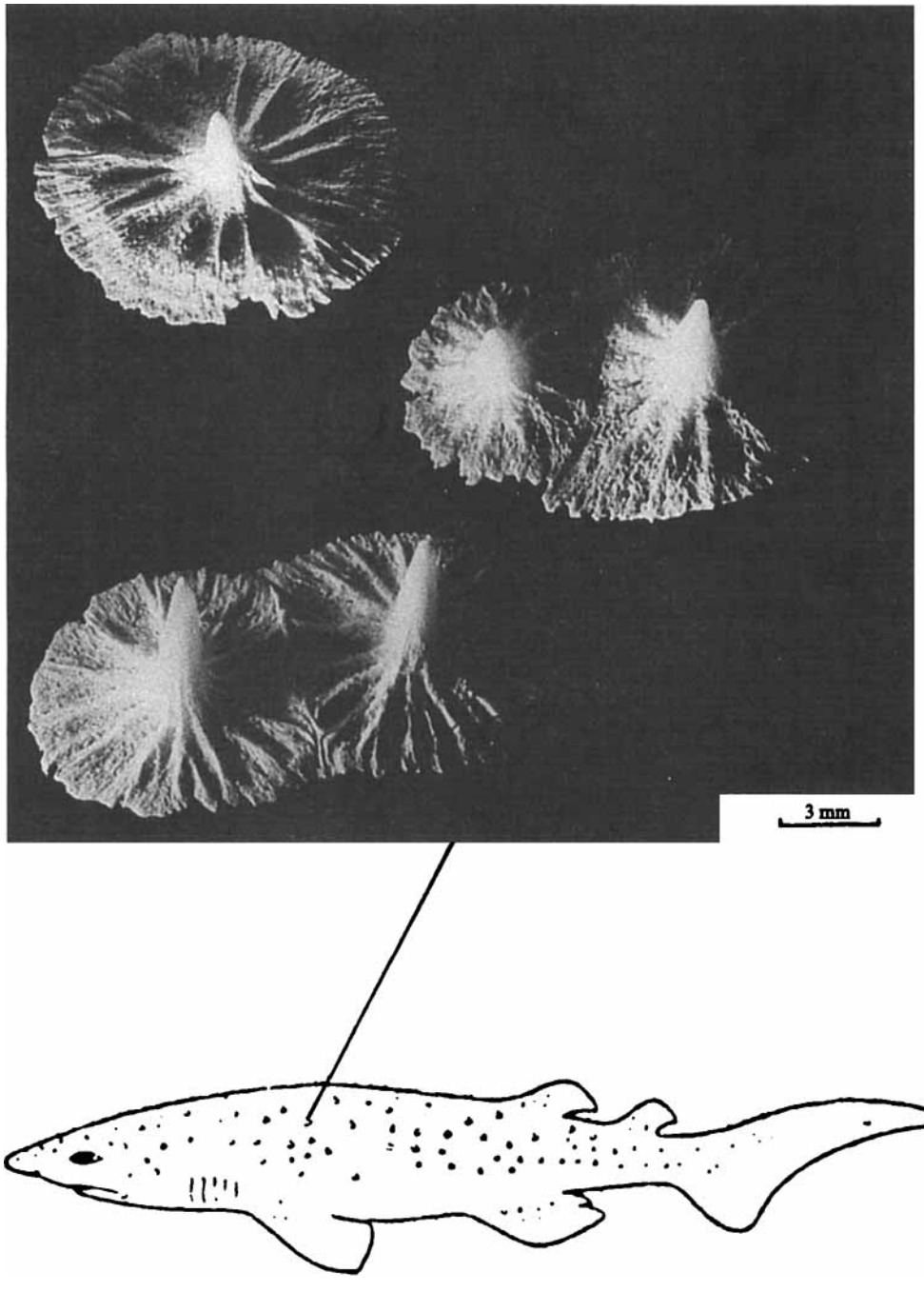

FIGURE 2. Bramble shark, *Echinorhinus brucus*, 1.90 m length.

This is a perturbation pattern which is found quite frequently in turbulent boundary layers. For instance, at an isolated roughness element on a smooth surface, such a flow pattern can be studied in detail, most clearly in the idealized case where this obstacle is immersed in a laminar boundary layer (Acarlar & Smith 1987). Tempting as it may be, we shall not enter here the discussion on the appropriate interpretation

of the events that have been observed in a turbulent boundary layer. However, we would like to stress that it is sufficiently well documented that there is a streaky structure in the viscous sublayer and that this streaky structure has a preferred lateral wavelength. This observation has led to attempts to influence the flow structure by surfaces with ribs. To our knowledge, the first such attempt has been made in the investigation by Liu, Kline & Johnston (1966). The underlaying idea of some of the following investigations was also to achieve *drag reduction* with such non-planar surfaces. Eventually, this goal was reached with very fine ribs (riblets) mainly due to the careful and systematic work carried out at NASA Langley during the last decade (Walsh 1980, 1982, 1983, 1984; Wilkinson & Lazos 1987). At about the same time, work in Germany which was actually induced by the observation of shark skin by W.-E. Reif and A. Dinkelacker, led to similar results (Nitschke 1983; Dinkelacker, Nitschke-Kowsky & Reif 1987). A drag reduction, i.e. a turbulent shear stress reduction, of about 4–7 % below that of a smooth flat plate was achieved. There is no ambiguity any more about this finding, because a similar drag reduction has been documented by various other research groups, e.g. by Bechert, Hoppe & Reif (1985), Van Dam (1986), Sawyer & Winter (1987), Choi (1987), McLean, George-Falvy & Sullivan (1987), and others. Besides that, successful applications on competition boats have been reported and have caused some publicity.

However, we are still far away from really understanding the operation mechanism of riblet surfaces. In addition, we do not know whether 7 % is the maximum drag reduction that can be achieved with non-planar surfaces. In previous papers (Bechert *et al.* 1985; Bechert *et al.* 1986) we have suggested a number of hypotheses on the actual operation of shark scales, which may lead beyond this limit. At the present time, however, there is no direct experimental evidence available to prove that this would actually extend the range of turbulent drag reduction. In this paper, by contrast, we shall confine ourselves to the theoretical investigation of the viscous sublayer on surfaces with long straight ribs aligned in the streamwise direction. There were two reasons for this research. (i) It is important to know the location of the origin of a turbulent boundary layer on a riblet surface. (ii) It may be possible that this viscous flow calculation provides some hints for an improved configuration of a drag-reducing riblet surface.

2. Basic considerations

One of the unsettled questions concerning riblet surfaces was where the average origin of the velocity profile might be located. This question was raised in the paper by Hooshmand, Youngs & Wallace (1983) and we suggested in a previous paper (Bechert *et al.* 1985) that this problem could be solved by a viscous flow theory. Figure 3 shows the apparent (or average) origin of the velocity profile which lies below the tip of the rib and above the bottom of the valley between the ribs. We call the distance between apparent origin and rib tip the *protrusion height*, because it determines how far the rib tips protrude into the boundary layer.

We consider the average mean flow of the viscous sublayer in which the riblet surface is immersed. In the following equations we choose x as the direction of the mean flow, y as the direction normal to the surface and z as the lateral direction. We start with the first Navier–Stokes equation

$$\frac{\partial u}{\partial t}+u\frac{\partial u}{\partial x}+v\frac{\partial u}{\partial y}+w\frac{\partial u}{\partial z}+\frac{1}{\rho}\frac{\partial p}{\partial x}=\nu\nabla^2 u. \tag{1}$$

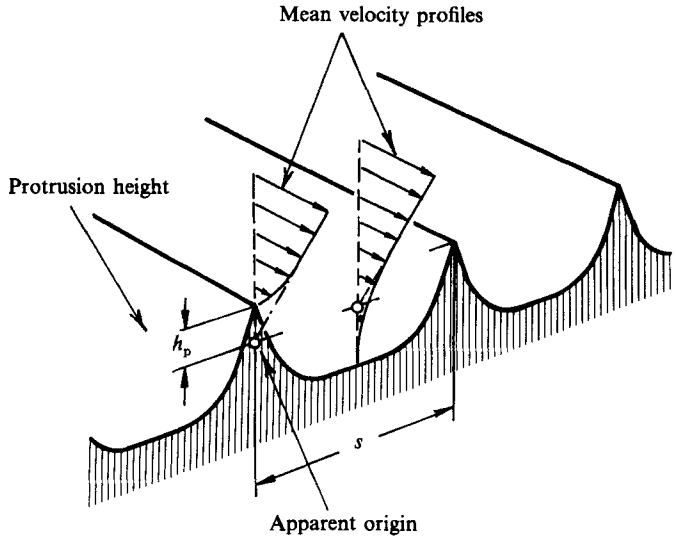

FIGURE 3. Apparent origin of a riblet surface.

Obviously, for a mean flow calculation, the first term of the equation can be omitted. If the riblet surface is completely immersed in the viscous sublayer, neglecting the convective terms on the left-hand side of the equation is certainly a good approximation. In fact, previous experiments do show that the relevant parameter regime where drag reduction occurs corresponds to the situation where this condition is just fulfilled. We shall return to this issue more explicitly in the discussion (§10) at the end of this paper. We assume a flat-plate boundary-layer flow without mean flow pressure gradient, so $\partial p/\partial x = 0$. For 'two-dimensional' riblets which do not vary in cross-section in the streamwise direction, we are left with the equation

$$\frac{\partial^2 u}{\partial y^2} + \frac{\partial^2 u}{\partial z^2} = 0, \tag{2}$$

which is a Laplace equation for the velocity u. To solve this equation in two dimensions, various established techniques can be used. One particularly suitable one is conformal mapping. This technique has two striking advantages: (i) Sharp edges which produce singularities in the flow field do not lead to problems or inaccuracies with this method whereas, for example, purely numerical methods would encounter such problems. (ii) For a variety of configurations, solutions in closed form can be worked out. In particular, simple formulae for the protrusion height can be produced.

Conformal mapping utilizes the fact that for the Laplace equation (2) arbitrary functions $f(z+iy)$ are solutions. The function f, the mapping function, has to be selected so that the boundary condition on the riblet surface is $u = 0$. The mean flow u-distribution will be a uniform Couette shear flow in order to emulate the viscous sublayer. What we shall do by conformal mapping is to transform a uniform shear flow above a smooth plane surface into that above the particular riblet surface. So the task is to do mathematically what is shown in figure 4. By the way, the solid lines in figure 4 are *not* streamlines, but lines of constant velocity u (isotaches). In conformal mapping we usually plot the real and imaginary part of a function, so we obtain a network with lines intersecting each other perpendicularly. If the imaginary

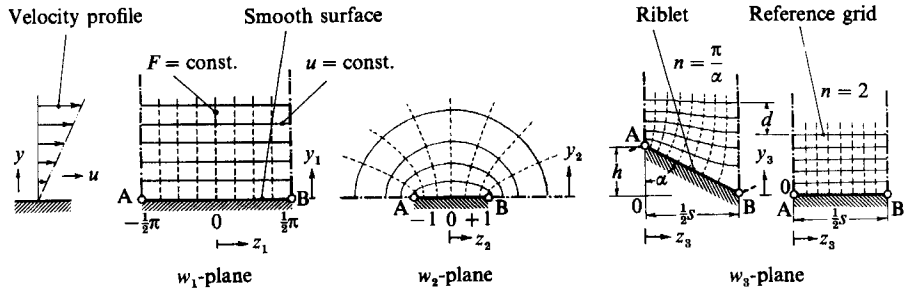

FIGURE 4. Conformal transformations leading to the viscous flow on a sawtooth riblet surface.

part of our function is u, what is then the significance of the real part, i.e. the broken lines in figure 4? The answer is simple: between two broken lines a shear force

$$\Delta F = l\tau_0 \Delta z \tag{3}$$

is transmitted. In (3), l is the length in the streamwise (x) direction and Δz is the spacing between two broken lines of the undisturbed grid far above the riblet surface. τ_0 is the shear stress $\tau_0 = \mu\, \mathrm{d}u/\mathrm{d}y$, where $\mathrm{d}u/\mathrm{d}y$ is the velocity gradient above the smooth surface or far away from the riblet surface. Thus, we call the broken vertical lines in figure 4 *force lines* (isodynes).

3. Riblets with a sawtooth profile

Riblet surfaces with a sawtooth-like cross-section have been extensively tested by Walsh (1980, 1982, 1984) and they do produce drag reduction in a turbulent boundary layer. Therefore, we have chosen this configuration as a first example in our viscous flow analysis. The procedures of the conformal transformations are as follows (see figure 4):

(*a*) A rectangular grid of velocity lines and force lines in the w_1-plane ($w_1 = z_1 + \mathrm{i}y_1$) is fixed. The vertical extension of the grid is chosen from $y_1 = 0$ to an arbitrary upper value, and the horizontal extension of z_1 is from $-\frac{1}{2}\pi$ to $+\frac{1}{2}\pi$.

(*b*) This grid is transformed by the mapping function sinus, i.e. $w_2 = \sin w_1$.

(*c*) The half-plane above a straight horizontal line can be transformed into the plane inside a polygon by virtue of the Schwarz–Christoffel transformation. For details on this technique see, for example, the books of Betz (1964) and Kober (1957).

The Schwarz–Christoffel transformation provides the mapping function to relate the w_3-plane to the w_2-plane:

$$\frac{\mathrm{d}w_3}{\mathrm{d}w_2} = C_1 \frac{1}{(w_2+1)^{\alpha/\pi}} \frac{1}{(w_2-1)^{(\pi-\alpha)/\pi}}. \tag{4}$$

C_1 is a constant and the integration of (4) will produce another constant, C_2. These two constants have to be determined later. α is the corner angle of the polygon (see figure 4). In order to carry out the integration, it is useful to introduce the following substitution:

$$\xi = \left(\frac{w_2-1}{w_2+1}\right)^{\frac{1}{n}} \quad \text{with} \quad \frac{1}{n} = \frac{\alpha}{\pi}. \tag{5}$$

We obtain

$$w_3 = nC_1 \int \frac{\mathrm{d}\xi}{1-\xi^n} + C_2. \tag{6}$$

This integration can be carried out for n being an integer number (see Gradstein & Rhyshik 1981). For $n = 4$ ($\alpha = 45°$), we obtain, for example,

$$w_3 = \tfrac{1}{2}s\left[1 + \frac{\mathrm{i}}{\pi}\left(\ln\frac{1+\xi}{1-\xi} + 2\arctan\xi\right)\right] \tag{7}$$

with $\xi = (w_2 - 1/w_2 + 1)^{\frac{1}{4}}$. For this case, the constants had been determined as

$$C_1 = \frac{\mathrm{i}s}{2\pi}, \quad C_2 = \tfrac{1}{2}s \tag{8}$$

in order to obtain a grid pattern with dimension and orientation in figure 4.

For other angles, the mapping function can become more cumbersome. However, we have worked out the mapping functions for:

n	3	4	6	8
α	60°	45°	30°	22.5°
ridge angle	120°	90°	60°	45°

The formulae of the mapping functions are given in the Appendix. The grid pattern, i.e. the velocity distributions and the force lines are given in figure 5. These drawings are computer plots of our equations. The reference grid can be seen on the right-hand side of each plot in figure 5. The apparent origin, i.e. the location of an equivalent smooth surface, corresponds to the lowest horizontal line with zero velocity of this reference grid. Several things become obvious from these plots: (i) The velocity perturbations caused by the riblet structure are vanishing very rapidly with increasing distance from the riblet surface. (ii) There is very little fluid motion and extremely low shear stress at the bottom of the grooves, in particular for the smaller riblet angles. (iii) The protrusion height h_p does not seem to increase above a certain fraction of the riblet spacing s.

This latter observation can be quantified further. We find through the coordinate transformations where the different points A and B move for a riblet surface, in comparison to the undisturbed reference pattern (represented by $\alpha = 90°$ or $n = 2$). In this way, we can derive a general formula for the protrusion height h_p for arbitrary riblet angles. The details of this calculation are given in a previous conference paper (Bechert *et al.* 1986). We find

$$\frac{h_p}{s} = \frac{1}{2\pi}\left\{\gamma + 2\ln 2 + \frac{\pi}{\tan\alpha} - \frac{\pi}{\alpha} + \psi\left(1 + \frac{\alpha}{\pi}\right)\right\} \tag{9}$$

In this equation, γ is the Euler constant $\gamma = 0.5772$ and ψ is the Digamma function, as defined and tabulated in the tables of Abramovitz & Stegun (1972). In figure 6 we have plotted (9) for the protrusion height versus the height of the riblets. Both quantities have been made dimensionless with the riblet spacing s. For low values of the relative riblet height h/s, the protrusion height is half the riblet height, i.e. $h_p \approx \frac{1}{2}h$. For high riblets, however, there is a saturation of the protrusion height at $h_{p_{max}} = 0.2206s$. This saturation limit ($0.2206 = \ln 2/\pi$) is an important and unexpected finding of this paper. We shall see in the next section whether this limit value is also valid for other configurations.

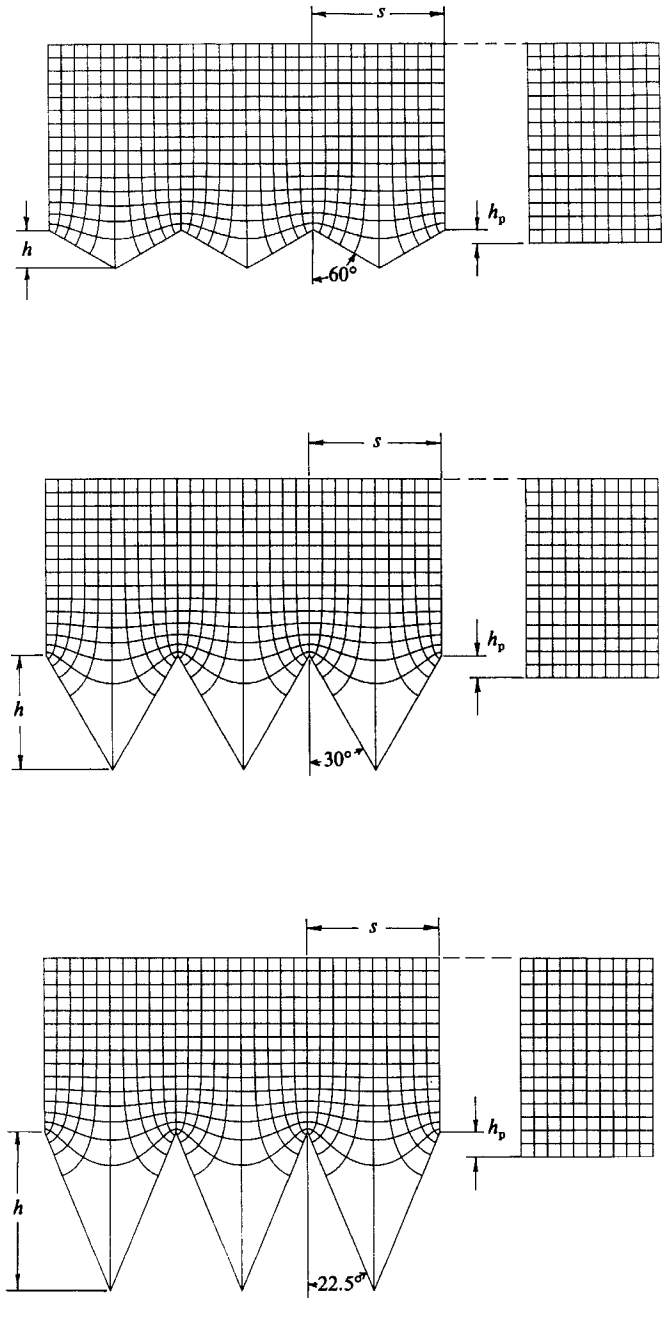

FIGURE 5. u-velocity and fluid shear force distribution of the viscous flow on a sawtooth riblet surface for various riblet angles.

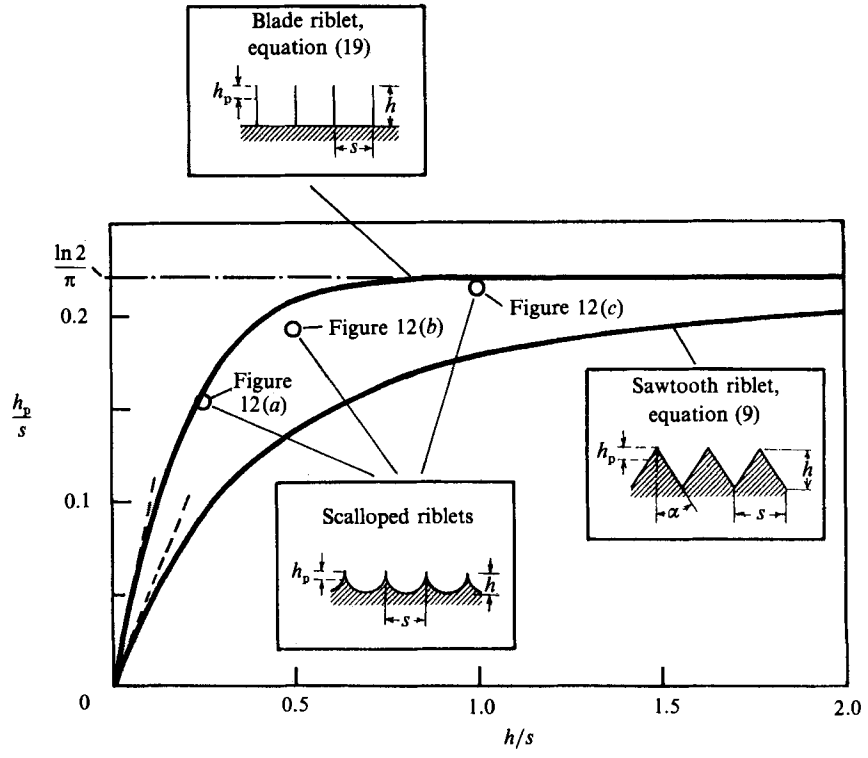

FIGURE 6. Protrusion height h_p as a function of geometrical height h for various types of riblets.

4. Riblets with trapezoidal grooves

For trapezoidal grooves, the Schwarz–Christoffel transformation again provides the mapping function in order to relate the w_3-plane to the w_2-plane. However, this time we have one more corner in the configuration. This produces (see Kober 1957) one more term in the denominator of the mapping function corresponding to (4) in the preceding section. To integrate this equation is somewhat cumbersome. The details of this calculation are given in Bartenwerfer & Bechert (1987). The protrusion height can be expressed in terms of Gamma functions and Hypergeometric functions. We have evaluated these functions numerically and the computed curves are quite easy to understand (see figure 7). Of course, the data for the trapezoidally grooved riblets must lie between the sawtooth riblets of the preceding section and thin blade-like riblets, which we shall calculate with an independent approach in the following section.

In addition, we have evaluated an asymptotic equation for the protrusion height h_p for small riblet height h:

$$\frac{h_p}{s} \sim \left(1-\frac{s_r}{s}\right)\frac{h}{s}+\frac{s_r}{s}\frac{h}{2s}, \tag{10}$$

with s_r being the width of the foot of the rib (see figure 7). For $h/s > 1$ we have another approximate formula, which is essentially an interpolation between the asymptote of the blade riblet and the curve of the sawtooth riblet:

$$\frac{h_p}{s} \sim \left(1-\frac{s_r}{s}\right)\frac{\ln 2}{\pi}+\frac{s_r}{2\pi s}\left[\gamma+2\ln 2+\frac{\pi}{\tan\alpha}-\frac{\pi}{\alpha}+\psi\left(1+\frac{\alpha}{\pi}\right)\right]. \tag{11}$$

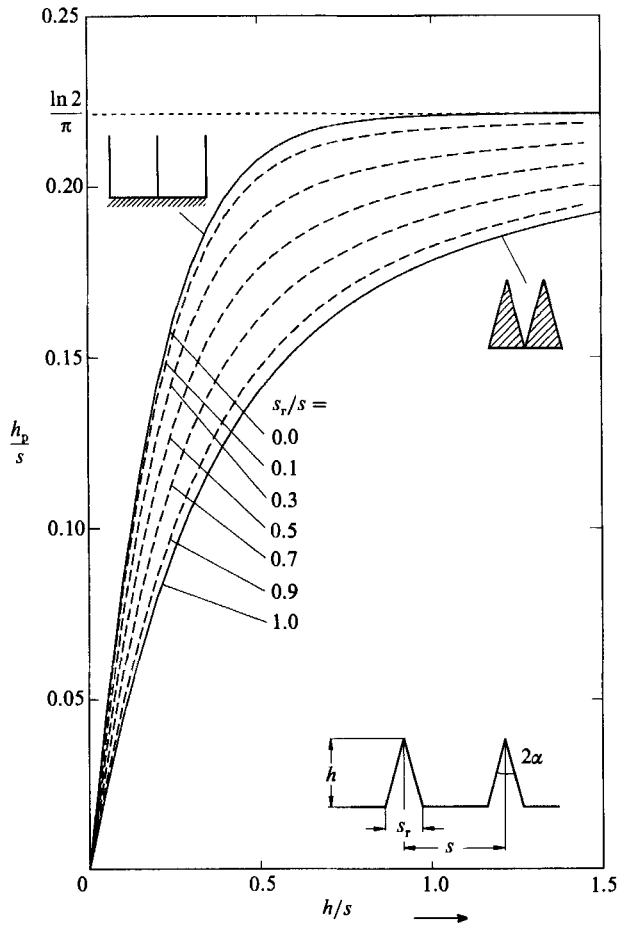

FIGURE 7. Protrusion height h_p as a function of geometrical height h for riblets with trapezoidal valleys. The riblet foot breadth s_r is kept constant for each curve.

Another probably more useful way to plot the data in figure 7 can be seen in figure 8. Here, for each individual curve, the rib tip angle is kept constant and the depth of the grooves is varied. For small groove depth all curves behave like blade riblets. On the other hand, the asymptotic value of h_p/s for deep grooves is given by the data of the sawtooth riblet. The asymptotic protrusion height for deep grooves is reached at a groove depth h/s between 0.4 and 0.6. Therefore, a groove deeper than $h/s \approx 0.6$ has no influence whatsoever.

We have also worked out an approximate equation for the asymptotic value of h_p/s with the rib tip angle being kept constant:

$$\left(\frac{h_p}{s}\right)_{max} \sim \frac{\ln 2}{\pi}\left(1 - 1.25\frac{\alpha}{\pi}\right), \tag{12}$$

valid for $h/s > 0.6$ and $\alpha/\pi < 1/12$.

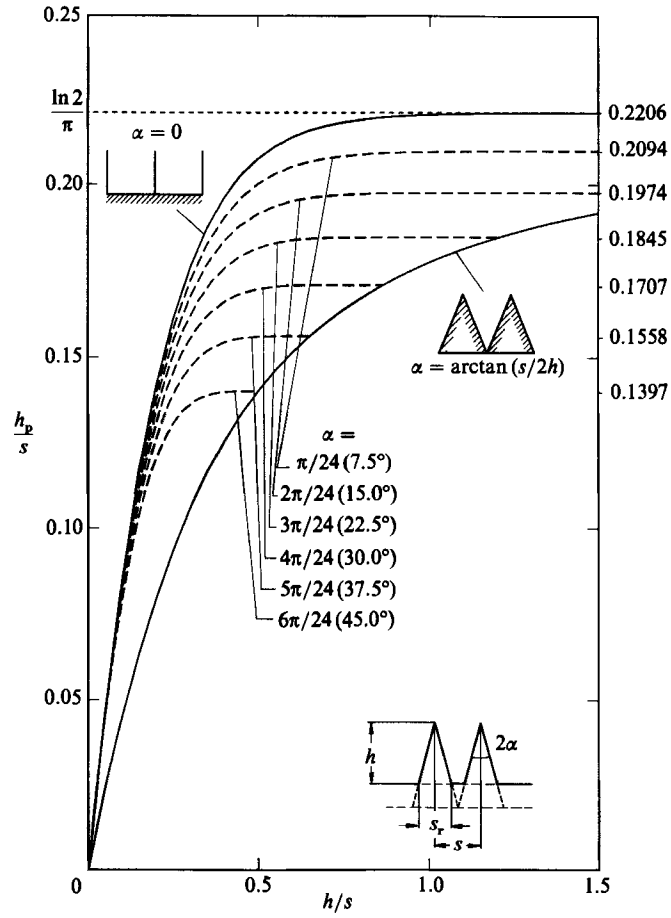

FIGURE 8. Riblets with trapezoidal valleys as in figure 7. The riblet tip angle is kept constant for each dashed curve.

5. Blade-shaped riblets

Two-dimensional blade-shaped riblets have been introduced by Wilkinson & Lazos (1987) as a drag-reducing surface. Therefore, we also carry out the viscous flow calculation for this configuration. As in the preceding section, the viscous flow on blade-shaped riblets can be calculated using the Schwarz–Christoffel transformation. In fact, a transformation with $n = 2$ (i.e. rectangular corners) and a shift in coordinates between the w_2- and the w_3-planes would do the job. However, the following procedure to solve the problem is different and resembles somewhat the procedure to calculate the flow in blade rows of turbomachines (Betz 1964). Its basic advantage is that it can be modified to deal with other configurations such as scalloped riblet shapes, which are found on shark scales.

If we use methods of turbomachinery flows, we may draw the reader's attention to an obvious fact: the grids representing lines of $u = \text{const}$ and $F = \text{const}$ look like streamlines $\Psi = \text{const}$ and potential lines $\Phi = \text{const}$ of a potential flow field. In spite of the fact that we do not really consider a stream in the (z, y)-plane we may, however, utilize this analogy. This has the advantage that, as fluid dynamicists, we are used to thinking in terms of streamlines. It is, for example, easy to see what a

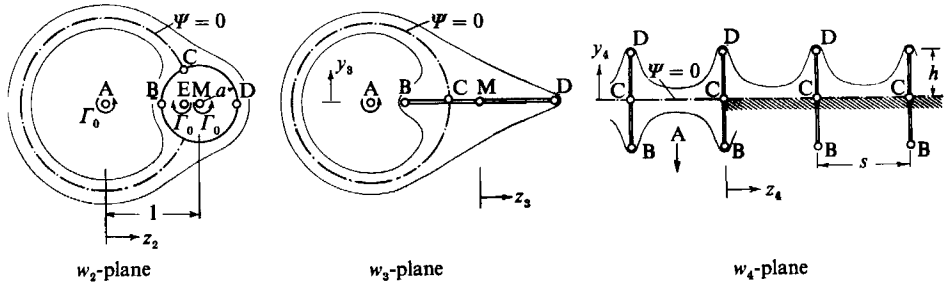

FIGURE 9. Conformal transformations leading to the viscous flow on a blade riblet surface.

stagnation point and a stagnation streamline in the (Ψ, Φ)-plane are. However, what would we call them in our (u, F)-plane? Thus, we shall use Ψ and Φ instead of u and F, intermediately. At the end of our calculations, we shall just change the names of the functions back to u and F, their real meaning.

In the (Ψ, Φ)-plane, the task is to find the potential flow around an array of blades. This task is carried out in several steps (see figure 9). The w_1-plane is not shown in figure 9. It is, as before, an undisturbed rectangular Ψ, Φ (or u, F) grid. The flow in the w_2-plane is the flow around a cylinder of radius a, induced by a vortex with strength Γ_0. The induced field of this vortex alone would be

$$\Phi + \mathrm{i}\Psi = \frac{\mathrm{i}\Gamma_0}{2\pi} \ln (z_2 + \mathrm{i}y_2). \tag{13}$$

In order to fulfil the no-penetration condition on the surface of the cylinder, we need a mirror-image vortex of identical strength Γ_0, but with negative sign, inside the cylinder at an eccentric location E. Having only these two vortices would produce a field with circles as streamlines everywhere. Also, as we would see later, the streamlines in the final w_4-plane would not be these of a horizontal parallel flow. This latter condition is fulfilled if we install an additional positive vortex of strength Γ_0 in the centre of the cylinder.

We shall not show all the details of the mathematics here. Since there are no unusual steps involved, we shall show only a few equations and outline the essential steps of the transformations. The stream function of the flow around the cylinder in figure 9, which is the stream function of the sum of the three vortices, is found to be

$$\Phi + \mathrm{i}\Psi = w_1 = \frac{\mathrm{i}\Gamma_0}{2\pi} \ln \left[\frac{w_2(w_2 - 1)}{w_2 - 1 + a^2} \right], \tag{14}$$

where $w_2 = z_2 + \mathrm{i}y_2$. The radius of the cylinder is a and the distance between the origin at A (where the inducing vortex is located) and the centre of the cylinder at M has been set equal to one.

The streamlines can be calculated by inverting (14) to find w_2 at a given w_1. Since (14) is a quadratic equation for w_2, this is a straightforward procedure. By following one $\Psi = \text{const.}$ line through the w_2-plane, one can decide which one of the two solutions of the quadratic equation is to be chosen.

The next step is to 'smash' the cylinder in figure 9 to obtain a single blade of finite

length. The transformation capable of doing that is well known from airfoil theory, i.e. the Kutta–Joukowsky transformation

$$w_3 = w_2 + \frac{a^2}{w_2}. \tag{15}$$

Before we apply this transformation, however, we have to shift the origin of the coordinate system from A to the centre of the cylinder, M. Thus, with the appropriate adjustment of constants, we have instead of (15)

$$w_3 = (w_2 - 1) + \frac{a^2}{(w_2 - 1)} + 1 + a^2. \tag{16}$$

After having applied the Kutta–Joukowsky transformation, the point A has moved a bit to the left and, interestingly, the stagnation streamline $\Psi = 0$ still remains a circle.

Before performing the next step, we move the origin back to the (shifted) centre of the inducing vortex, A. By applying the transformation $\ln w$ we obtain the desired periodical flow pattern on the blade row. With the proper choice of constants, the transformation equation is

$$w_4 = \frac{is}{2\pi} \ln\left(\frac{w_3}{1 - a^2}\right), \tag{17}$$

where s is the riblet spacing. The result of this transformation can be seen in figure 9. The broken line is the stagnating streamline $\Psi = 0$ and is equivalent to the location of the wall with $u = 0$. The height of the riblets can be controlled by changing the radius a of the circle in the w_2-plane (see figure 9). After some intermediate calculations, one can find the relation that determines the riblet height h:

$$\frac{h}{s} = \frac{1}{\pi} \operatorname{arctanh} a. \tag{18}$$

With the above outlined procedure, a set of flow patterns has been calculated for various riblet heights, see figure 10.

The protrusion height h_p is the height of the riblet h minus the upwards shift of the streamlines (lines of constant u) in the w_4-plane of figure 9. Its magnitude can be determined by carefully determining the locations of the points in the different planes after the different transformations. We find after some intermediate calculations

$$\frac{h_p}{s} = \frac{1}{\pi} \ln\left(1 + \tanh\left(\frac{\pi h}{s}\right)\right). \tag{19}$$

From (19), one can see, that $h_p \approx h$ for small h/s. This means that, for very small blade riblets, the protrusion height is equal to the real height of the blade riblets.

On the other hand, for large blade heights, the blade riblets behave like the sawtooth riblets, see figure 6. This is because for very deep grooves only the top of the blade takes the viscous force. Obviously, the top of the blade is identical for deep grooves on sawtooth riblets and on blade riblets. Thus, the limit value for the protrusion height is again $h_p/s \to \ln 2/\pi$ for large h/s.

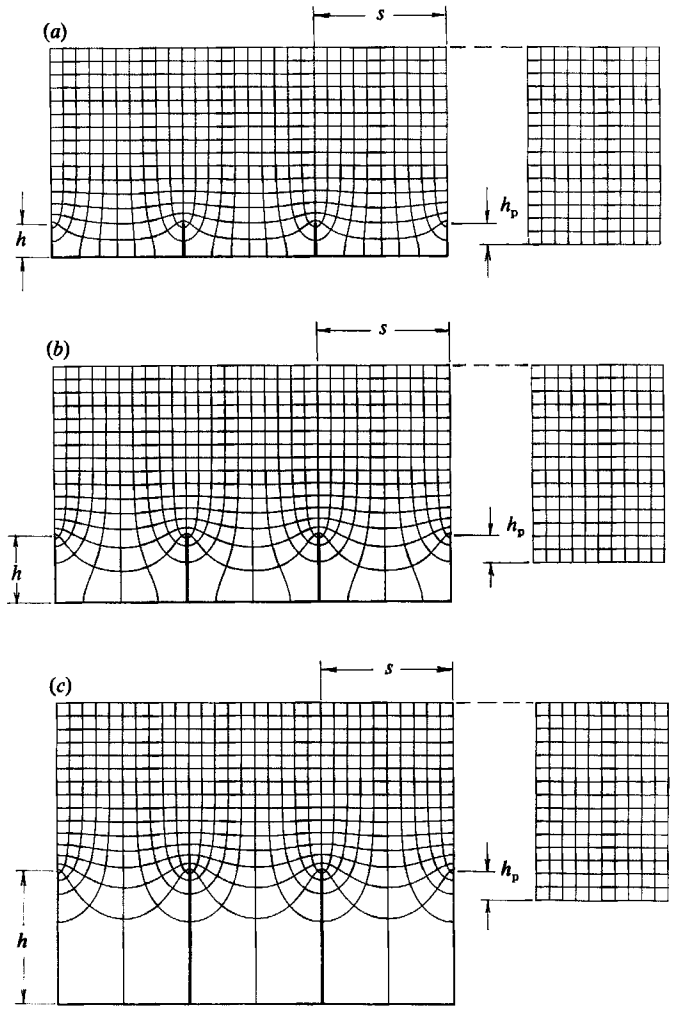

FIGURE 10. u-velocity and fluid shear force distribution of the viscous flow on blade riblet surfaces for various riblet heights: (a) $h/s = 0.25$; (b) 0.5; (c) 1.0.

6. Scalloped riblets

Riblets with scalloped cross-section are found on the scales of fast sharks. In laboratory experiments, it has been shown that scalloped riblets with semicircular shape match the best sawtooth riblets, with a drag reduction of 7% (Walsh 1982; Bechert *et al.* 1985). The viscous flow calculation on these scalloped riblets can be carried out with a modification of the transformations that we used for blade riblets.

The Kutta–Joukowsky transformation in the preceding section (equation (15)) had a constant a equal to the cylinder radius a. We obtain scalloped riblets if this radius of the mapping circle, which we call now b, is larger than the cylinder radius a, see figure 11. In addition, the mapping circle is no longer coaxial with the cylinder. The position of the mapping circle has to be chosen so that it touches two streamlines with the same value (Ψ_c), but opposite sign, at the horizontal axis, $y_2 = 0$. The streamlines between $-\Psi_c$ and $+\Psi_c$ penetrate into the blade in the w_3- and w_4-planes. In the final plane, w_4, the Ψ_c streamlines become the scalloped wall contour of the

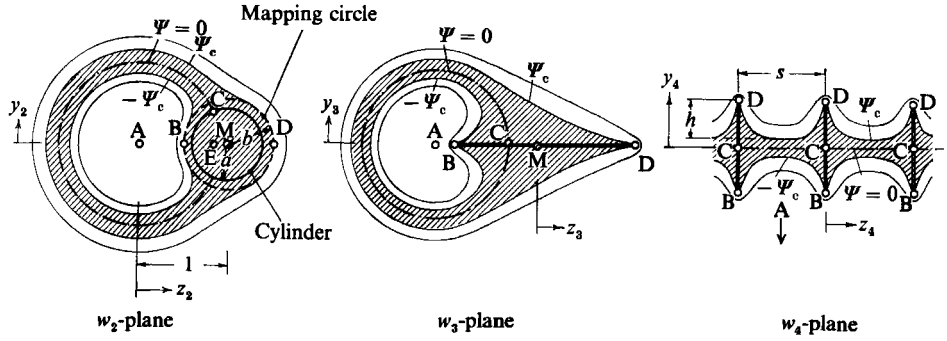

FIGURE 11. Conformal transformation leading to the viscous flow distribution on a riblet surface with scalloped cross-section.

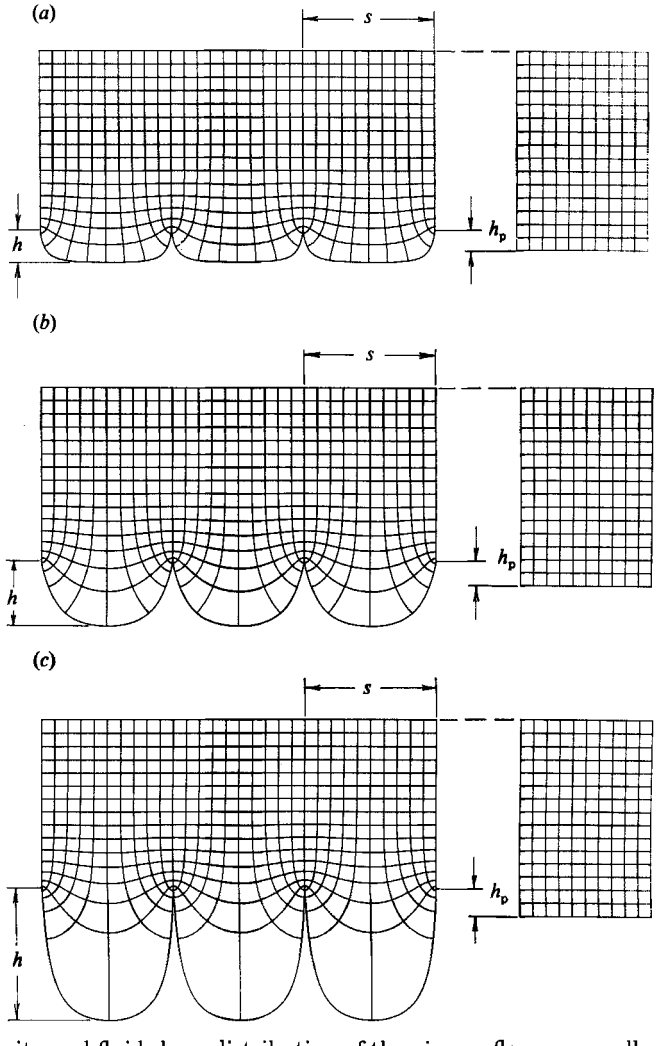

FIGURE 12. u-velocity and fluid shear distribution of the viscous flow on a scalloped riblet surface. (*a*) Riblet height $h/s = 0.25$, parameter $a/b = 1.155$, protrusion height $h_p/s = 0.155$. (*b*) Scalloped riblet with nearly semicircular cross-section. Riblet height $h/a = 0.50$, parameter $a/b = 1.192$, protrusion height $h_p/s = 0.192$. (*c*) Scalloped riblet; height $h/s = 1.00$, parameter $a/b = 1.0325$, protrusion height $h_p/s = 0.216$.

riblets. By numerical trial, cylinder radius and mapping circle radius can be adjusted so that the riblet contour is very close to a semicircle. This particular configuration and its flow distribution is shown in figure 12(*b*). Of course, the velocity value on the surface has to be readjusted so that $u = 0$ at the contour Ψ_c. In this particular case, the protrusion height is $h_p/s = 0.192h/s$. Other scalloped surfaces and their flow distributions are given in figure 12(*a*, *c*). In general, the protrusion height of scalloped riblets lies between sawtooth riblets and blade-shaped riblets. But, as one can see from figure 6, they can indeed be very close to blade riblets. Of course, mechanically, scalloped riblets are much more durable than blade riblets.

7. Rounded ridges

In technological applications of riblet surfaces, the wedge at the tip of the riblet will never be sharp with a radius of curvature equal to zero, as assumed in the preceding examples. Thus, it is important to know what the influence of a *finite* radius of curvature may be.

Similarly to the preceding modification of the mapping function which produced scalloped riblets, one can modify the Kutta–Joukowsky transformation into the other direction, which is more familiar from airfoil theory. If one chooses a mapping circle radius smaller than the cylinder radius, one obtains 'club'-like blade riblets with rounded edges, see figure 13. Also the modified flow pattern can be seen in the example calculated in figure 13.

The calculations, which are given in more detail in Bartenwerfer & Bechert (1987), clearly show that there is a dramatic decrease of the protrusion height h_p caused by a finite radius of curvature R_k at the rib wedge. A sample of our calculated examples of club-like riblets is given in figure 14. For small R_k/s we found an approximate equation, which shows the decrease of h_p/s (as compared to the protrusion height for infinitely small radius of curvature)

$$\frac{h_p}{s} \approx \frac{h_p}{s}\bigg|_{R_k=0} - \frac{\tanh^{\frac{3}{4}}(\pi h/s)}{2\pi}\left(\frac{\pi R_k}{s}\right)^{\frac{1}{2}}. \tag{20}$$

As one sees from this equation or from figure 14, one loses about 10% of the protrusion height if the radius of curvature on the rib tip is only 0.5% of the lateral rib spacing. If one relates the protrusion height to the maximum thickness t of the club-like wedges (see figure 13), one can compile another approximate equation from our numerical data†

$$\frac{h_p}{s} \approx \frac{h_p}{s}\bigg|_{R_k=0}\left(1 - \frac{2t}{s}\right). \tag{21}$$

The value of $(h_p/s)|_{R_k=0}$ can be taken from (19). Equation (21) is valid for $t/s < 0.1$ and $0.5 \leqslant h/s \leqslant 1.0$.

One may consider our club-like riblets as too artificial and restricted in their shape. Of course, there are also other ways to generate rib shapes with rounded tips. One such possibility is this: we take the flow distribution above thin blade-like riblets as considered in the preceding section, for example, those in figure 10. We choose a line $u = \text{const.}$ above the actual surface and consider this as the new surface. Obviously, this produces a variety of riblet surfaces with rounded edges. Our numerical data

† This equation is identical to equation (23) in our Bechert *et al.* 1986, but it deviates by the coefficient 2 from (76) in our previous report (Bartenwerfer & Bechert 1987) where this latter equation is mistyped.

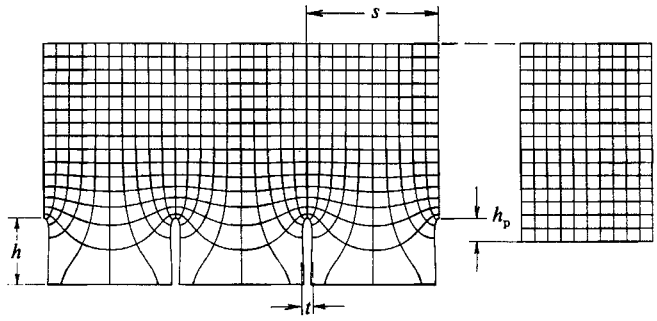

FIGURE 13. Blade riblet with rounded edge: configuration and flow distribution. Riblet height $h/s = 0.50$, parameter $a/b = 0.773$, protrusion height $h_p/s = 0.179$, maximum thickness $t/s = 0.0740$.

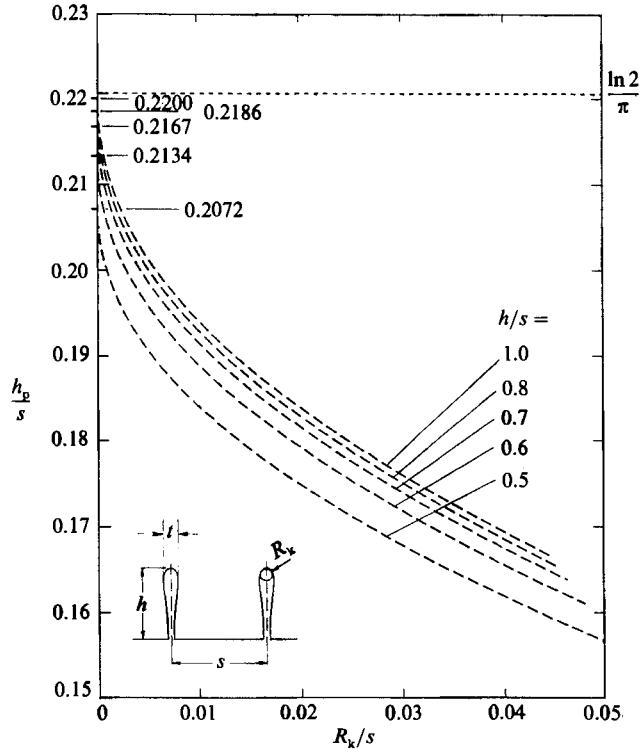

FIGURE 14. Influence of the tip radius of curvature R_k on the protrusion height h_p of club-like riblets for various riblet heights h.

indicate a law very similar to that of (20). However, these data can be collapsed best if one multiplies the second term on the right-hand side of (20) with the coefficient 1.3.

This additional enhancing coefficient reflects the fact that, with increasing radius of curvature, the wedge angle of the riblets is also increased, which further decreases the protrusion height (see §4 on trapezoidally grooved surfaces).

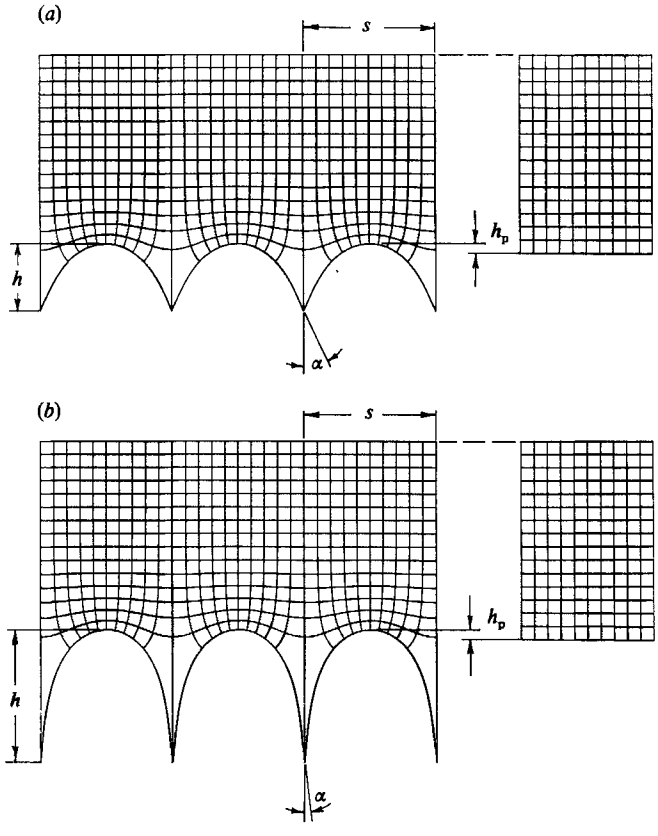

FIGURE 15. Convex riblet, u-velocity and shear force distribution. (a) Riblet height $h/s = 0.50$, parameter $\alpha/\pi = 0.1305$, protrusion height $h_p/s = 0.0724$. (b) Riblet height $h/s = 1.00$, parameter $\alpha/\pi = 0.0275$, protrusion height $h_p/s = 0.0767$.

8. Convex riblets

The mathematical methods in the preceding section are unable to produce convex riblets with, say, semicircular shape. However, experiments with these configurations have been carried out (Walsh 1982) and thus we were also interested in this configuration.

Owing to a programming error in our data plotting program for sawtooth riblets, we ran inadvertently into the solution of this problem. Consider the mapping function, (7) in §3. By omitting the second term we obtain

$$w_3 = \tfrac{1}{2}s\left(1+\frac{\mathrm{i}}{\pi}\ln\frac{1+\xi}{1-\xi}\right); \quad \text{with} \quad \xi = \left(\frac{w_2-1}{w_2+1}\right)^{\frac{1}{n}}. \tag{22}$$

Instead of the originally expected pattern, we get the viscous flow above two convex riblets per division s. By varying the parameter $n = \pi/\alpha$ in the function ξ of (22), we can vary the depth of the grooves. Figures 15(a) and 15(b) show the viscous flow on convex riblets, calculated with the mapping function (22), the grid size being normalized to obtain one riblet per division s.

The protrusion height can be calculated for each pattern. It is $h_p/s = 0.0724$ for figure 15(a) and 0.0767 for figure 15(b). For convex riblets, the protrusion height is always very small.

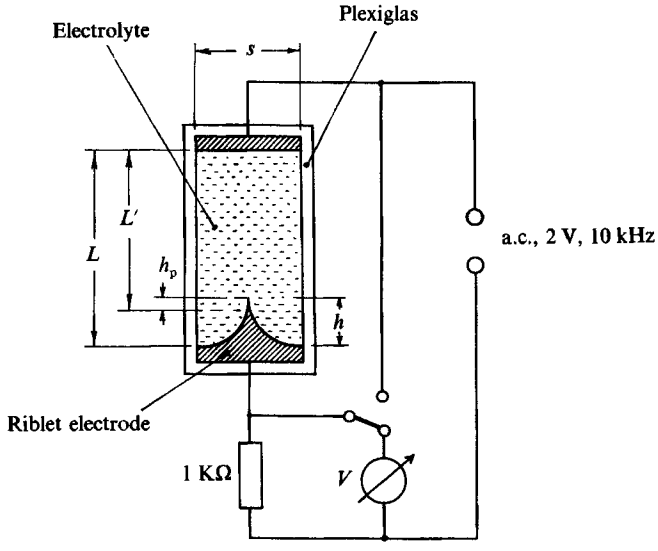

FIGURE 16. Schematic diagram of the electrolytic experiment.

9. Electrolytic experiments

It appeared desirable to also be able to determine the protrusion height for riblet configurations with shapes different from the ones already considered. For this purpose we devised a simple experimental technique. In addition, this will provide an independent proof for our theoretical calculations. It is well known that the electric field in a conductor, for example, an electrolyte, obeys the same Laplace equation as a potential flow does. Obviously, this method is also applicable to our viscous flow problem. In the model experiment, lines of constant velocity u would correspond to lines of constant voltage V in an electrolytic tank. However, besides obtaining velocity distributions using a point probe, we can also easily measure the protrusion height. For this latter purpose we have established a measuring set-up which is shown schematically in figure 16. We measure the resistance R of the rectangular electrolytic tank without and with the riblet electrode via a voltage measurement. The resistance of the tank without the riblet electrode is proportional to the length L of the tank. The decrease in the resistance caused by the presence of the riblet electrode is equivalent to a decreased length L' of the electrolyte. We have

$$L-L' = h-h_p \tag{23}$$

and

$$h_p = h-(L-L'), \tag{24}$$

where h_p is the protrusion height and h is the geometrical height of the riblet, as before. The shape of the riblet electrode has to be chosen so that the walls of the rectangular tank are symmetry planes.

The electrolytic measurements of the protrusion height h_p/s plotted versus the geometrical height h/s can be seen in figure 17. The agreement clearly shows that our calculations are correct. There is, however, a systematic deviation: the measurements on the blade riblets show a protrusion height about 5% lower than the theoretical values. We assume that this minor discrepancy is caused by the finite thickness of the blades of the blade riblet electrodes. The blade thickness is $t = 0.025s$. Then our

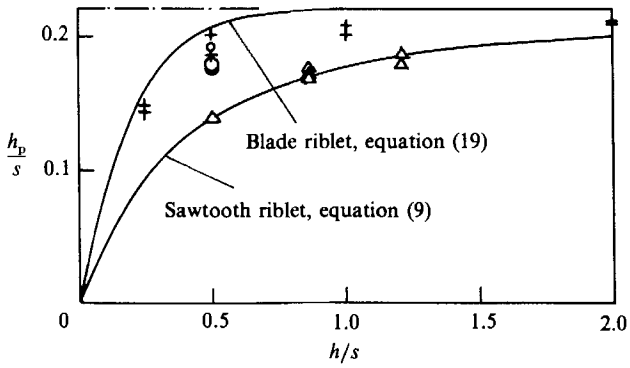

FIGURE 17. Protrusion height. Electrolytic experiments versus theory. Experiment: △, sawtooth riblet; +, blade riblet. Semicircular riblet: ○, theory; ○, experiment.

approximate formula for the decrease of the protrusion height, (20), would predict a decrease of 5%. Thus, the discrepancy is explained.

The reader who is interested in the technical details of the experiment is referred to our previous conference paper on this issue (Bechert *et al.* 1986).

10. Discussion

In this final section we shall try to establish a connection between our viscous flow calculations and the issue of turbulent shear stress reduction by riblet surfaces. Since that problem as a whole cannot be solved analytically at the present time, this part of the paper will contain both proven and other still hypothetical material. Having carried out numerous experiments on turbulent drag reduction, we are modest enough to admit that many of our previous plausible-looking ideas have failed. Thus, we are aware of the possibility that some of our present opinions may change in the future. However, what we conclude below is compatible with the data available to us at the present time.

(i) Our theoretical calculations are certainly valid under purely viscous flow conditions. However, it took us some time to convince ourselves that such a theory is also useful for a prediction of the viscous sublayer flow in a turbulent boundary layer. In fact, for the parameter regime where drag reduction occurs, the riblet surface is actually almost completely imbedded in the viscous sublayer. To give an example: we consider sawtooth riblets with riblet height equal to lateral riblet spacing (Walsh 1982). There, the optimal lateral spacing is about $s^+ = 15$. s^+ is given in 'wall units', i.e. s is made dimensionless with the shear stress velocity $[\tau_0/\rho]^{\frac{1}{2}}$ and the kinematic viscosity ν. Thus $s^+ = s[\tau_0/\rho]^{\frac{1}{2}}/\nu$ with τ_0 being the shear stress of the smooth reference plate under otherwise identical flow conditions. The protrusion height for this geometry is $h_p = 0.18s$ (see figure 6) or $h_p^+ = 2.7$. Thus, the rib tips protrude only 2.7 wall units above the origin of the velocity profile. By all available definitions of the thickness of the viscous sublayer ($y^+ = 5$, or $y^+ = 3$ for the 'linear sublayer') this means that the riblets are imbedded in the viscous sublayer. Also, hot-wire data of mean flow quantities on riblet surfaces (Wallace 1987) support our approach. Clearly, our calculations can be valid only within a regime very close to the riblet surface.

(ii) We would like to stress that our calculation cannot predict quantitatively any turbulent shear stress reduction by riblet surfaces. It can only predict the velocity

and shear stress distribution once the average shear stress is known. An integration of the shear stress distribution on a riblet surface using our theory is possible, but will lead to the trivial result that the average shear stress is given by the slope of the Couette flow above the riblets.

(iii) The merit of our calculations is, however, that the *origin* of the velocity profile can be predicted. The origin lies below the rib tips, usually at a distance of 10–20% of the rib spacing. This distance, which we call the *protrusion height* h_p, cannot exceed 22% of the lateral rib spacing ($0.22 = \pi^{-1} \ln 2$).

(iv) The above-mentioned limit of the protrusion height is valid only for that class of configurations where the tip of the rib looks, with increasing groove depth, more and more like a thin blade. Thus, this limit is valid for sawtooth riblets, blade riblets, riblets with trapezoidal grooves and riblets with scalloped cross-section. Configurations that are altogether different, for example, thin wires stretched above a smooth plate (suggested by Kramer 1939) are likely to have also a different limit for the protrusion height.

(v) The determination of the origin of the velocity profile is not only of academic interest. For instance, for experiments with riblet surfaces inside tubes, it is important to know the effective inner diameter of the tubes. Without knowledge of this effective inner diameter, it would be hard to make any statements about friction losses in tubes with riblets.

(vi) We think that the method of conformal mapping to incorporate the boundary conditions of riblet surfaces may be valuable for further work in this field. For instance, the viscous sublayer model of Pearson (1988) utilizes this approach. Furthermore, for numerical computations with the full Navier–Stokes equations, it is desirable to have an orthogonal grid with a high resolution in the critical regions, i.e. close to the rib tips. Our conformal mapping grids do have exactly that property and may thus turn out to be useful for numerical computations.

We feel, however, that there should be a connection between our calculation and the ability of riblet surfaces to decrease turbulent shear stress. Our basic hypothesis is that sharp ribs do impede the instantaneous crossflow in the viscous sublayer, which is generated by the turbulent motion. In this way the whole turbulent momentum exchange in the boundary layer is also reduced, which is equivalent to a shear stress reduction. This should occur if the rib tips protrude sufficiently above the origin of the velocity profile. More insight into the mechanism can be obtained from a discussion of the experiments by Wilkinson & Lazos (1987). A schematic survey of their experiments can be seen in figure 18. Blade-shaped riblets with different ratios h/s, i.e. height to lateral spacing, have been tested. On the vertical axis τ/τ_0 is plotted, the ratio of the turbulent shear stress of the riblet surface to that of the smooth surface. On the horizontal axis, the dimensionless riblet spacing s^+ is plotted. The protrusion height is calculated from (21), taking the finite thickness of the ribs into account. The data in figure 18 show an increase of drag if the blades protrude too far into the boundary layer. For lower values of the dimensionless protrusion height h_p^+, drag reduction occurs. For sparse blades (see curve with $h/s = 0.153$), little effect on the flow is exerted. The more blade there are, the higher is the effect on the flow (see curve with $h/s = 0.797$). Our viscous calculation, however, tells us that the protrusion height, and with it the effect on the cross-flow, finally decreases if the blades are too close to each other. From these considerations, it emerges that the protrusion height seems to have some relation to the ability of riblets to impede the cross-flow. Roughly speaking, this ability should depend on how far the ribs stick out from the surface, which indeed points to the protrusion height.

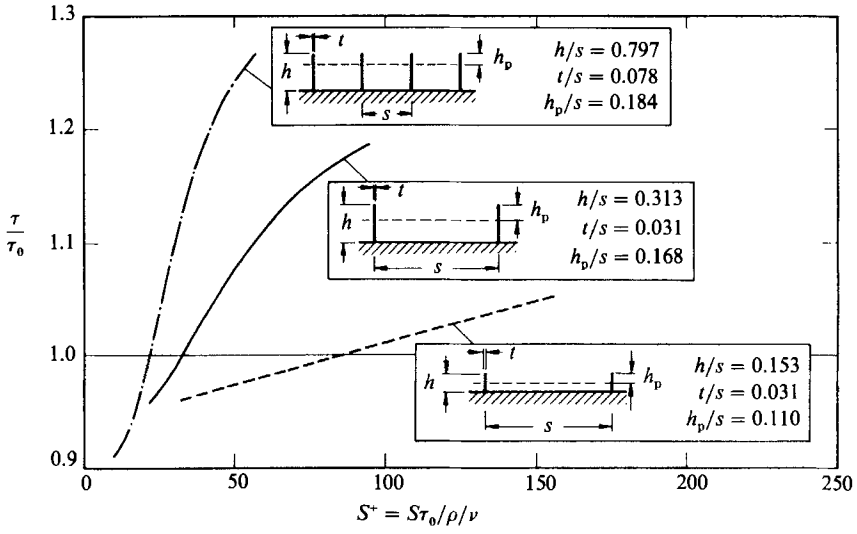

FIGURE 18. Turbulent shear stress on blade-shaped riblets, according to Wilkinson & Lazos (1987).

At first glance, there seems to be a contradiction between this suggestion and the observation (see figure 18) that the ribs should not protrude too far into the turbulent regime. However, given a maximum admissible protrusion height in terms of h_p^+, it is easy to see that we can accommodate more ribs in the lateral direction if the ratio h_p/s is maximal. This, again, points to a high h_p/s. At the present time, there is no piece of experimental evidence available to us that contradicts this concept. In fact, there are several previous experiments that support our point of view: (i) convex riblets do not produce drag reduction (Walsh 1982); (ii) riblets with a very shallow groove exhibit only a very small drag reduction (Walsh 1980); (iii) from Walsh's (1982) and our own experimental data we know that riblets that do not have really sharp wedges are inferior in their drag reducing ability.

Given this guideline, and using our viscous flow calculations, an optimal riblet configuration should have:

(i) a sharp wedge for the rib, preferably with a radius of curvature smaller than 0.5–1% of the lateral rib spacing;

(ii) a rib wedge angle as small as possible; and

(iii) a valley depth of about 60% of the lateral rib spacing.

At the present time, mainly sawtooth riblets with an h/s ratio (height to rib spacing) of unity are used. Also, the wedge angle of these sawtooth shapes of about 55° seems perhaps too high. The riblet configuration which we found on the scales of the Silky Shark (*Carcharhinus falciformis*) seems to us optimal in the light of the above considerations. It has a scalloped cross-section with a groove depth h/s of 0.5–0.6 and very sharp ridges with a wedge angle of about 30°. On the other hand, we are aware of the fact that our suggested optimal riblet configuration would promise only a modest improvement of the protrusion height and, with it, hopefully, the drag-reducing performance.

We appreciate the numerous valuable suggestions on our manuscript by Dr S. Schümmelpult and Professor H. Hahnebüch.

Appendix. Transformation functions for various ridge angles of sawtooth riblets

Note that in all cases $w_2 = \sin w_1$ and $\xi = (w_2 - 1/w_2 + 1)^{1/n}$ (equation (5)).

(i) Normalized undistorted grid $n = 2; \alpha = 90°$

$$w_3 = \tfrac{1}{2}s\left[1 + \frac{\mathrm{i}}{\pi}\ln\frac{1+\xi}{1-\xi}\right] = \frac{s}{2\pi}(w_1 + \tfrac{1}{2}\pi). \tag{A 1}$$

(ii) $n = 3$; $\alpha = 60°$; ridge angle = 120°

$$w_3 = \tfrac{1}{2}s\left[1 + \frac{\mathrm{i}}{\pi}\left(\ln\frac{(1+\xi+\xi^2)^{\frac{1}{2}}}{1-\xi} + \sqrt{3}\arctan\frac{2\xi+1}{\sqrt{3}} - \sqrt{3}\arctan\frac{1}{\sqrt{3}}\right)\right]. \tag{A 2}$$

(iii) $n = 4$; $\alpha = 45°$; ridge angle = 90°

$$w_3 = \tfrac{1}{2}s\left[1 + \frac{\mathrm{i}}{\pi}\left(\ln\frac{1+\xi}{1-\xi} + 2\arctan\xi\right)\right]. \tag{A 3}$$

(iv) $n = 6$; $\alpha = 30°$; ridge angle = 60°

$$w_3 = \tfrac{1}{2}s\left[1 + \frac{\mathrm{i}}{\pi}\left(\ln\frac{1+\xi}{1-\xi} - \tfrac{1}{2}\ln\frac{\xi^2-\xi+1}{\xi^2+\xi+1} + \sqrt{3}\arctan\frac{2\xi-1}{\sqrt{3}} + \sqrt{3}\arctan\frac{2\xi+1}{\sqrt{3}}\right)\right] \tag{A 4}$$

(v) $n = 8$; $\alpha = 22.5°$; ridge angle = 45°

$$w_3 = \tfrac{1}{2}s\left[1 + \frac{\mathrm{i}}{\pi}\left(\ln\frac{1+\xi}{1-\xi} - \frac{1}{\sqrt{2}}\ln\frac{\xi^2-\sqrt{2}\,\xi+1}{\xi^2+\sqrt{2}\,\xi+1} + 2\arctan\xi + \sqrt{2}\arctan(\sqrt{2}\,\xi-1) + \sqrt{2}\arctan(\sqrt{2}\,\xi+1)\right)\right]. \tag{A 5}$$

REFERENCES

ABRAMOVITZ, M. & STEGUN, I. A. 1972 *Handbook of Mathematical Functions*. Dover.

ACARLAR, M. S. & SMITH, C. R. 1987 A study of hairpin vortices in a laminar boundary layer. Part 1. Hairpin vortices generated by a hemisphere protuberance. *J. Fluid Mech.* **175**, 1–41.

BARTENWERFER, M. & BECHERT, D. W. 1987 Die viskose Strömung über Oberflächen mit Längsrippen. DFVLR-FB 87-21. (English transl. The viscous flow on surfaces with streamwise aligned riblets. ESA-TT-1091 1988.)

BECHERT, D. W., BARTENWERFER, M., HOPPE, G. & REIF, W.-E. 1986 Drag reduction mechanisms derived from shark skin. *15th Congr. of the Int. Counc. of the Aeronautical Sciences, Sept. 7–12, 1986, London, Paper* ICAS-86-1.8.3. AIAA.

BECHERT, D. W., HOPPE, G. & REIF, W.-E. 1985 On the drag reduction of the shark skin. *AIAA*-Paper 85-0546.

BETZ, A. 1964 *Konforme Abbildung*. Springer.

BURDAK, V. D. 1969 Function of the ctenoid apparatus of fish in the presence of a turbulent boundary layer. *Zoologichevskiy Zhurnal* **48**, 1053–1055 (in Russian).

CHERNYSHOV, O. B. & ZAYETS, V. A. 1970 Some peculiarities of the structure of the skin of sharks. In *Hydrodynamic Problems of Bionics*. Bionica Nr. 4, pp. 77–83 (in Russian).

CHOI, K. S. 1987 Test of drag reducing riblets on a one-third scale racing yacht. *Proc. Turbulent Drag Reduction by Passive Means, Royal Aeronautical Society, 15–17 Sept., London.*

COLES, D. 1978 A model for flow in the viscous sublayer. *Proc. Coherent Structures of Turbulent Boundary Layers. AFOSR/Lehigh Workshop 1978*, pp. 462–475.

CORRSIN, S. 1956 Some current problems in turbulent shear flows. *Symp. on Naval Hydrodynamics, Washington, DC, 24–28 Sept., 1956. Publ.* 515, National Academy of Sciences-National Research Council, 1957.

DINKELACKER, A., NITSCHKE-KOWSKY, P. & REIF, W.-E. 1988 On the possibility of drag reduction with the help of longitudinal ridges in the walls. *IUTAM Symp. on Turbulence Management and Relaminarization, Bangalore, India, Jan. 1987* (ed. H. W. Liepmann & R. Narasimha). Springer.

GRADSTEIN, I. S. & RYSHIK, I. M. 1981 *Tables of Series, Products, and Integrals.* (Transl. from Russian.) Frankfurt: Harri Deutsch.

HOOSHMAND, D., YOUNGS, R. & WALLACE, J. M. 1983 An experimental study of changes in the structure of a turbulent layer due to surface geometry changes. *AIAA-paper* 83-0230.

JANG, P. S., BENNEY, D. J. & GRAN, R. L. 1986 On the origin of streamwise vortices in a turbulent boundary layer. *J. Fluid Mech.* **169**, 109–123.

KLINE, S. J., REYNOLDS, W. C., SCHRAUB, F. A. & RUNSTADLER, P. W. 1967 The structure of turbulent boundary layers. *J. Fluid Mech.* **30**, 741–773.

KOBER, H. 1957 *Dictionary of Conformal Representations.* Dover.

KRAMER, M. 1939 Einrichtung zur Verminderung des Reibungswiderstandes. Reichspatentamt, Patentschrift Nr. 669897, Klasse 62b, Gruppe 408. Patentiert vom 17.März 1937 an.

LIU, C. K., KLINE, S. J. & JOHNSTON, J. P. 1966 An experimental study of turbulent boundary layer on rough walls. *Stanford University, Dep. Mech. Eng., Rep.* MD-15, July 1966.

MCLEAN, J. D., GEORGE-FALVY, D. N. & SULLIVAN, P. P. 1987 Flight-test of turbulent skin-friction reduction by riblets. *Proc. Turbulent Drag Reduction by Passive Means, the Royal Aeronautical Society, 16–17 Sept., London.*

NITSCHKE, P. 1983 Experimentelle Untersuchung der turbulenten Strömung in glatten und längsgerillten Rohren. *Max-Planck-Institut für Strömungsforschung, Göttingen. Bericht* 3/1983. (Trans.: Experimental investigation of the turbulent flow in smooth and longitudinally grooved tubes. *NASA TM* 77 480, 1984.)

PEARSON, C. F. 1988 Interaction of streamwise vorticity with a grooved boundary. *Bull. Am. Phys. Soc.*, **33**, 2233.

RASCHI, W. G. & MUSICK, J. A. 1984 Hydrodynamic aspects of shark scales. *Virginia Institute of Marine Science, Gloucester Point, Va. 22062, Rep.* 272, Jan. 1984.

REIF, W.-E. 1982 Morphogenesis and function of the squamation in sharks. *Neues Jahrbuch für Geologie und Palaentologie, Abhandlungen Band* 164, pp. 172–183. Stuttgart: E. Schweizerbart'sche Verlagsbuchhandlung.

REIF, W.-E. 1985 Squamation and ecology of sharks. *Courier Forschungsinstitut Senckenberg*, Frankfurt/M., Nr. 78, 255 p.

REIF, W.-E. & DINKELACKER, A. 1982 Hydrodynamics of the squamation in fast swimming sharks. *Neues Jahrbuch für Geologie und Palaentologie, Abhandlungen Band* 164, pp. 184–187. Stuttgart: E. Schweizerbart'sche Verlagsbuchhandlung.

SAWYER, W. G. & WINTER, K. G. 1987 An investigation of the effect on turbulent skin friction of surfaces with streamwise grooves. *Proc. Turbulent Drag Reduction by Passive Means, Royal Aeronautical Society, London 15–17 Sept.*

SMITH, C. R. & METZLER, S. P. 1983 The characteristics of low-speed streaks in the near-wall region of a turbulent boundary layer. *J. Fluid Mech.* **129**, 27–54.

STEUBEN, K. S. & KREFFT, G. 1978 *Die Haie der Sieben Meere* (The sharks of the seven seas). Hamburg: Verlag Paul Parey.

VAN DAM, W. P. 1986 Weerstandsvermindering en een turbulente grenslag als gevolg van microgroeven. *Technische Hogeschool Delft, Vakgroep Stromingsleer, Rep.* June 1986.

VAN DYKE, M. 1982 *An Album of Fluid Motion.* Stanford: Parabolic.

WALLACE, J. M. 1987 On the mechanism of viscous drag reduction using streamwise aligned riblets: a review with some new results. *Proc. Turbulent Drag Reduction by Passive Means, Royal Aeronautical Society, 15–17 Sept., London.*

WALSH, M. J. 1980 Drag characteristics of V-groove and transverse curvature riblets. In: *Viscous Flow Drag Reduction* (ed. G. R. Hough), Progress in Astronautics and Aeronautics, vol. 72. AIAA.

WALSH, M. J. 1982 Turbulent boundary layer drag reduction using riblets. *AIAA-paper* 82-0169.

WALSH, M. J. 1983 Riblets as a viscous drag reduction technique. *AIAA J.* **21**, 485–486.

WALSH, M. J. 1984 Optimization and application of riblets for turbulent drag reduction. *AIAA-Paper* 84-0347.

WILKINSON, S. P. & LAZOS, B. S. 1987 Direct drag and hot-wire measurements on thin-element riblet arrays. *IUTAM Symp. on Turbulence Management and Relaminarization. Bangalore, India, Jan. 1987* (ed. H. W. Liepmann & R. Narasimha). Springer.